

# Rapidly Rotating Lenses: Repeating features in the lightcurves of short period binary microlenses

Matthew T. Penny,<sup>1\*</sup> Eamonn Kerins,<sup>1</sup> Shude Mao<sup>2,1</sup>

<sup>1</sup>*Jodrell Bank Centre for Astrophysics, The Alan Turing Building, School of Physics and Astronomy, The University of Manchester, Oxford Rd, Manchester, M13 9PL, UK*

<sup>2</sup>*National Astronomical Observatories, Chinese Academy of Sciences, A20 Datun Road, Chaoyang District, Beijing 100012, China*

Accepted 2011 July 7. Received 2011 July 5; in original form 2011 May 7

## ABSTRACT

Microlensing is most sensitive to binary lenses with relatively large orbital separations, and as such, typical binary microlensing events show little or no orbital motion during the event. However, despite the strength of binary microlensing features falling off rapidly as the lens separation decreases, we show that it is possible to detect repeating features in the lightcurve of binary microlenses that complete several orbits during the microlensing event. We investigate the lightcurve features of such Rapidly Rotating Lens (RRL) events. We derive analytical limits on the range of parameters where these effects are detectable, and confirm these numerically. Using a population synthesis Galactic model we estimate the RRL event rate for a ground-based and space-based microlensing survey to be  $0.32f_b$  and  $7.8f_b$  events per year respectively, assuming year-round monitoring and where  $f_b$  is the binary fraction. We detail how RRL event parameters can be quickly estimated from their lightcurves, and suggest a method to model RRL events using timing measurements of lightcurve features. Modelling RRL lightcurves will yield the lens orbital period and possibly measurements of all orbital elements including the inclination and eccentricity. Measurement of the period from the lightcurve allows a mass-distance relation to be defined, which when combined with a measurement of microlens parallax or finite-source effects, can yield a mass measurement to a two-fold degeneracy. With sub-percent accuracy photometry it is possible to detect planetary companions, but the likelihood of this is very small.

**Key words:** gravitational lensing: micro – celestial mechanics – binaries: general – planetary systems – Galaxy: bulge

## 1 INTRODUCTION

By monitoring hundreds of millions of stars towards the Galactic bulge and Magellanic clouds, Gravitational microlensing surveys such as OGLE (Udalski 2003) and MOA (Hearnshaw et al. 2006) detect  $\sim 1000$  microlensing events per year. The lightcurves of most microlensing events follow the typical Paczyński (1986) form of a point-mass lens with a point source. However, many event lightcurves have a more complex form due to the effects of a binary or planetary companion to the lens (Mao & Paczyński 1991; Gould & Loeb 1992), a binary companion to the source (Griest & Hu 1992), microlens parallax (Refsdal 1966; Gould 1992), finite-source size (Gould 1994; Witt & Mao 1994; Nemiroff & Wickramasinghe 1994), or a combination of such. These effects provide additional information about the lens, such as the mass ratio and pro-

jected separation in binary or planetary lens events, or mass-distance relationships with parallax or finite-source effects. Measurement of both the finite-source size and microlensing parallax allow the lens mass to be solved for uniquely (Gould 1992), and if these occur in a binary or planetary lensing event, also allow measurement of the companion mass.

The complexities of microlensing lightcurves, to a greater or lesser extent, can all be considered as deviations from the single lens Paczyński form. The deviations may be relatively minor and can cover the entire lightcurve, as in most parallax events (e.g. Smith et al. 2002a), or they can be large and cover only a small fraction of the lightcurve, as in many binary lens events (e.g. Kubas et al. 2005; Beaulieu et al. 2006). In binary lens events, these deviations from the single lens form are caused by a difference in the magnification pattern of the lens. The most prominent ‘features’ of the binary lens magnification pattern are caustics, where the magnification of a point source diverges (see Figure 1). A source passing over a caustic will show a

\* mpenny@jb.man.ac.uk

sharp rise in its magnification as it enters it and a sharp fall as it leaves. Other, more smooth magnification pattern ‘features’ can be associated with the caustics in some way.

The caustic features of a binary lens magnification pattern are a natural feature of the binary lens mapping

$$z_s = z - \frac{1}{1+q} \left( \frac{1}{z - \bar{z}_1} + \frac{q}{z - \bar{z}_2} \right), \quad (1)$$

which maps the angular position of the source to image positions under the influence of the lens, and where we have used complex coordinates (e.g.  $z = x + iy$ , Witt 1990); bars represent complex conjugation,  $z_s$  is the position of the source,  $z$  the position of the image,  $z_1$  and  $z_2$  the positions of the primary and secondary lens components respectively, and  $q = M_2/M_1$  is the mass ratio of the lens components. All angles have been normalized to the Einstein ring radius

$$r_E = \frac{r_E}{D_1} = \frac{1}{D_1} \sqrt{\frac{4G}{c^2} x(1-x) D_s M}, \quad (2)$$

where  $r_E$  is the physical Einstein radius,  $D_1$  and  $D_s$  the distance to the lens and source respectively,  $M = M_1 + M_2$  is the total lens mass,  $x = D_1/D_s$  is the fractional lens distance, and  $G$  and  $c$  are the gravitational constant and speed of light respectively. The magnification  $\mu$  of an image is given by the determinant of the Jacobian of the lens mapping

$$\mu = \frac{1}{\det J}. \quad (3)$$

The magnification diverges when  $\det J = 0$ , and the solutions of this equation form smooth, closed curves in the image plane called critical curves, which when mapped back to the source plane form closed, cuspy curves: the caustics (see Figures 1 and 8).

In a binary lens event, the caustics are largest when the projected lens separation  $s = |z_2 - z_1| \sim 1$ , i.e., the lens components orbit with semimajor axis  $a \sim r_E \sim 2\text{--}3$  au. At these separations there is only a single, so-called resonant, caustic. Lenses with wider separations have two caustics, while those with closer separations have three (Schneider & Weiss 1986). The caustics of close and wide systems have smaller caustics than resonant systems, and so the source is less likely to encounter them. Far from the caustics, the binary lens features tend to be weak, and therefore, the lightcurves of binary lenses with very close or very wide orbits (which have correspondingly very small caustics), in most cases, will be indistinguishable from those of a single lens (e.g. Gaudi & Gould 1997).

The binary lenses with the strongest lightcurve features, thus have orbital periods  $T \sim 1000$  d, much longer than the microlensing event timescale

$$t_E = \frac{r_E}{v_t} \sim 20\text{d}, \quad (4)$$

for a typical Galactic microlensing event, where  $v_t$  is the relative lens-source transverse velocity (source velocity). The lenses therefore complete only a small fraction of their orbit during the course of the microlensing event, and only a fraction of the events are expected to show detectable signs of orbital motion in their lightcurves (Gaudi & Gould 1997; Dominik 1998; Konno & Kojima 1999; Ioka et al. 1999; Rattenbury et al. 2002; Penny et al. 2011). Those events where it has been detected typically involve caustic crossings, because the sharp caustic crossing features on the

lightcurve allow precise timing, which can be used to constrain even small lens motions (Albrow et al. 2000; An et al. 2002; Gaudi et al. 2008; Ryu et al. 2010; Hwang et al. 2010; Skowron et al. 2011; Batista et al. 2011). In these events, the orbital motion has constrained the properties of the lens orbit, and in one case allowed the measurement of several orbital parameters (Bennett et al. 2010).

In a previous paper, we have shown that with accurate photometry and dense enough lightcurve coverage, it is possible to detect orbital motion in lenses with closer orbits, and weaker, smooth lightcurve features (Penny et al. 2011). Typically occurring in events with longer microlensing timescales,  $t_E \sim 100$  d, the shorter orbital periods means that the lens completes a much larger fraction of the orbit during the event. In this paper we investigate the extreme case, where the lens completes at least one orbit during the microlensing event. In events involving such rapidly rotating lenses, magnification pattern features can sweep over the source more than once, and if detected in the lightcurve, these repeating features allow an accurate measurement of the lens period. Knowledge of the period places constraints on the lens mass, and if combined with a measurement of the finite-source effect or parallax, can be used to measure the lens mass to a two-fold degeneracy (Dominik 1998).

We begin the paper by defining when a binary lens is a rapidly rotating lens in Section 2. In Section 3 we look at whether rapidly rotating lenses are detectable, and the rate at which they are expected to occur. In Section 4, we then look at what information can be gained from observing a rapidly rotating lens, and suggest a method for modelling such events. In two appendices we examine how rapidly rotating lenses affect the microlensed images, and introduce additional effects that can affect rapidly rotating lens lightcurves.

## 2 WHAT IS A RAPIDLY ROTATING LENS?

We define a rapidly rotating lens (RRL) to be a binary microlens, which if monitored continuously with suitable photometric accuracy, would guarantee that at least one feature of its magnification pattern would be seen to repeat at least once in its lightcurve, due to the lens orbital motion. This implies that the lens completes at least two orbits during the time in which its binary lensing features are detectable. We choose this definition over the more simple comparison of microlensing and orbital timescales (e.g.  $T < t_E$ ) because without detecting binary features it is impossible to measure the binary’s rotation. As mentioned in the previous section, the strength of binary features declines as the orbital separation and period decrease, so simply decreasing the period does not necessarily increase the prospects of detecting a repeated feature. A rapidly rotating lens must therefore compromise between a fast rotation rate and detectable binary lensing features.

Throughout the paper we shall focus on close topology lenses, which have separations  $s \lesssim 0.7$  (Schneider & Weiss 1986; Erdl & Schneider 1993), a choice we shall justify in Section 3. Figure 1 shows the magnification pattern of a close topology lens, and labels a number of features. The structure and features of the magnification pattern depend only on the projected separation of the lens components  $s$ ,

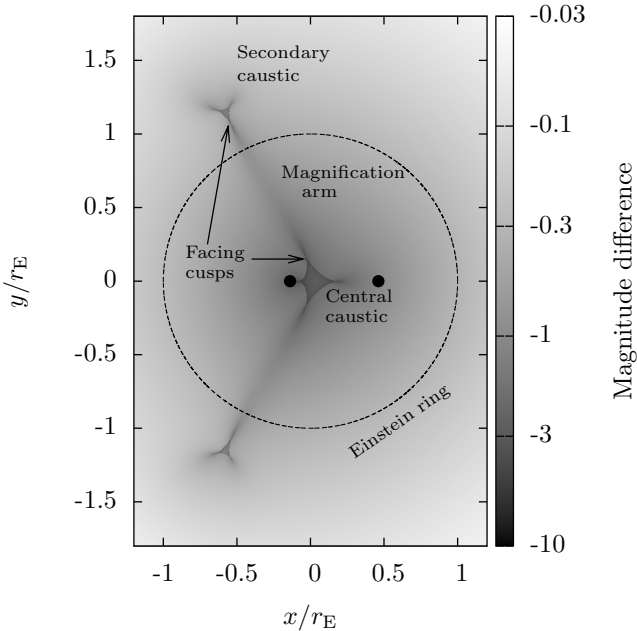


**Figure 1.** The magnification pattern of a close topology microlens. The dots denote the lens positions, with the primary lens at negative  $x$ . The lens has a mass ratio  $q = 0.3$  and projected separation  $s = 0.6$ . Notable features of the magnification pattern are labelled.

and the mass ratio  $q$  (Erdl & Schneider 1993). The most important features of the close magnification pattern are a central caustic, located at the lens centre of mass, and two secondary caustics which lie away from the lens centre. Stretched between the central and secondary caustics are two ‘arms’ of excess magnification (relative to the magnification that would be caused by a single lens of mass equal to the total binary mass). During a microlensing event, a source will travel across the magnification pattern, and we will observe the source to change in brightness, the form of this lightcurve being determined by the trajectory that the source takes. As the source moves, the magnification pattern will not stay fixed, as the binary will also move in its orbit. Should the lens orbit lie face-on to the line of sight, then the magnification pattern will rotate as the source moves across it. Should the orbit be inclined or eccentric, the structure of the magnification pattern will also change, as it depends on the projected lens separation  $s$  (Schneider & Weiss 1986).

Figure 2 shows the lightcurve (thick black line) of a RRL with a similar magnification pattern to that shown in Figure 1. It closely resembles the lightcurve of a single lens, the Paczyński lightcurve (grey line), but with a quasi-periodic variation over the entire lightcurve that only becomes obvious in the residual that is left once the Paczyński curve is subtracted from the lightcurve. These periodic features correspond to the magnification arms that extend between the secondary and central caustics, which sweep over the source as the lens rotates. The microlensing timescale of the lightcurve shown is  $t_E = 60$  d, but it is clear that repeating binary features remain in the lightcurve at time from peak magnification much greater than this, which corresponds to a source position far outside the Einstein ring. This is because the secondary caustics can lie far outside the Einstein

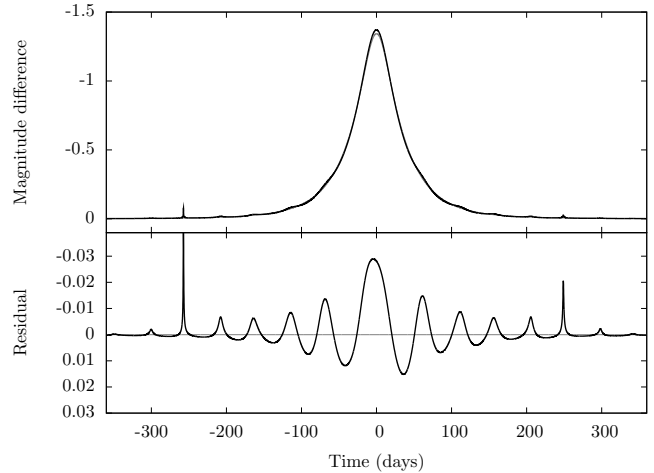


**Figure 2.** The lightcurve of a rapidly rotating lens. The upper panel shows the RRL lightcurve in black, and the Paczyński lightcurve of a single lens with the same total mass in grey. The lower panel shows the residual with respect to the Paczyński lens lightcurve. Features due to the magnification arms appear as peaks in the residual, while between them there are relative demagnifications. Large, short duration spikes occur when the secondary caustic passes close to or over the source. The system has parameters  $t_E = 61$  d,  $T = 92$  d,  $s = 0.23$ ,  $q = 0.8$ ,  $u_0 = 0.3$ ,  $\phi_0 = 1.75$  (see Section 4 for definitions of  $u_0$  and  $\phi_0$ ).

ring, their distance from the lens centre increasing as the binary separation decreases. However, their size, and the strength of the magnification arm connecting them with the central caustic, decrease with decreasing binary separation. We note at this point, that despite the large separation of the secondary caustics, we need not consider relativistic effects of superluminal caustics (Zheng & Gould 2000) as the ratio of the caustic rotational speed to the speed of light in all the cases we will consider is  $\sim 10^{-3}$ .

An RRL can clearly exhibit interesting, repeating lightcurve features if the binary period and separation conspire, but until now we have only considered RRLs in relation to parameters normalized to the typical microlensing length- and time-scales. In order to see if RRL events will be detectable in real microlensing surveys we must consider how their properties relate to the physical parameters of the lensing system.

### 3 ARE RRLS DETECTABLE?

In the previous section we defined a criterion for a lens to be a rapidly rotating lens, and described the features of an RRL event. In this section we put the definition on a more quantitative basis, and investigate whether RRLs will occur amongst the microlenses that are probed by microlensing surveys. To determine if detection is plausible, we investigate the range of physical parameters required to produce a microlensing event with repeating features, first analytically and then numerically. Finally we apply our numerical method to simulated microlensing surveys to estimate the expected rate of RRL detections.

### 3.1 An analytical approach

To see repeating features in a microlensing event, the most fundamental requirement of the system is that the lens completes more than one orbit during the event. The magnification pattern of a binary lens is complicated, but the essential features of a close binary lens can be captured by assuming it to be composed of two straight, radial arms that extend from the centre of mass to the position of the secondary caustics. Under this assumption, and assuming a random initial phase angle, repeating features are guaranteed to be observed if the lens completes two orbits in the time that the source spends within the radius swept out by the arms. We can write this as an inequality

$$2T < \frac{\pi}{2} u_{\pm} t_E, \quad (5)$$

where  $u_{\pm}$  is the radial position of the secondary caustics in units of Einstein radii (see Figure 8), and the factor of  $\frac{\pi}{2}$  is the mean chord length across a unit circle, and accounts for the random impact parameter of source trajectories relative to the lens centre of mass. It should be noted that it is possible for a feature to repeat if the binary completes between one and two orbits, but this requires a coincidence in the timing of the first feature.

Both the orbital period and the Einstein timescale depend on the lens mass, and the period also depends on the lens semimajor axis, so it is possible to write this constraint in terms of  $M$  and  $a$ . For projected lens separations  $s \ll 1$ , Bozza (2000) has derived an analytical approximation for the secondary caustic positions (see Equation 18), which if we keep only the first order terms is

$$u_{\pm}(s, q) \simeq s^{-1}. \quad (6)$$

Using equations 2 and 4 and Kepler's third law, with a little algebra we can then write Equation 5 as a constraint on the semimajor axis of the binary

$$a < 4.51 \text{ AU} [x(1-x)]^{2/5} D_s^{2/5} v_t^{-2/5} M^{3/5}, \quad (7)$$

where we have assumed a face-on orbit so that  $s = a/r_E$ , and where  $M$  is the total lens mass in solar masses,  $D_s$  the source distance in kpc,  $x \equiv D_l/D_s$  is the ratio of lens and source distances and  $v_t$  the relative lens-source velocity in  $\text{km s}^{-1}$ .

While we have an upper limit on the lens semimajor axis, in order to detect the RRL lightcurve features, they must be strong enough to be detectable in the photometry of the microlensing event. This requirement is somewhat ambiguous, but as the magnification pattern depends only on  $s$  and  $q$ , and the strength of features decreases with decreasing  $s$ , we can assume that for a given photometric precision and mass ratio, magnification pattern features will be detectable only when the separation is larger than a certain value, i.e.

$$s > s_{\text{det}}, \quad (8)$$

where  $s_{\text{det}}$  depends on  $q$  and the photometric accuracy. For stellar binary mass ratios, there will only be a small dependence on  $q$ , but there will be a strong dependence on the photometric accuracy; a value of  $s_{\text{det}} = 0.3$  is reasonable, however (see Section 3.2). We can again write this constraint as a limit on the semimajor axis

$$a > 2.85 \text{ AU} s_{\text{det}} [x(1-x)]^{1/2} D_s^{1/2} M^{1/2}. \quad (9)$$

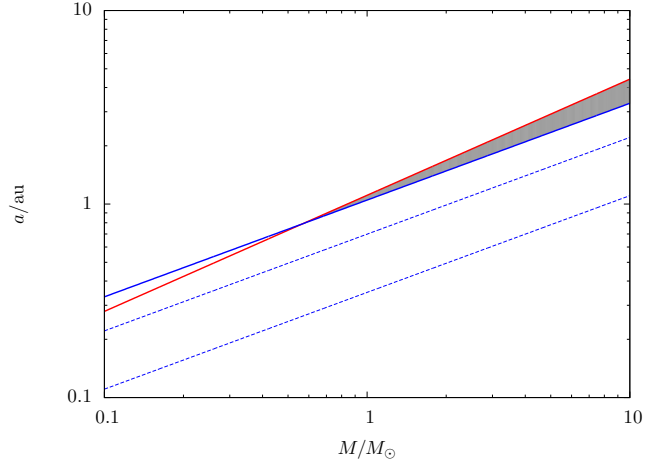


**Figure 3.** Plot showing the region of the total mass-semimajor axis plane where repeating features are observable. The red line shows the upper limit on  $a$ , provided by the constraint in Equation 7, while blue lines show the lower limit on  $a$ , provided by the constraint in Equation 9, with values of  $s_{\text{det}} = 0.3, 0.2$  and  $0.1$  from top to bottom. The other parameters are set at  $x = 0.75$ ,  $D_s = 8$  kpc and  $v_t = 50 \text{ km s}^{-1}$ . The region where repeating features are detectable for  $s_{\text{det}} = 0.3$  is shaded grey.

We now have two constraints on  $a$ , an upper and a lower limit, which are dependent on other parameters of the lensing system, the most interesting being the total lens mass. Figure 3 shows the two constraints on semimajor axis as a function of mass, for a lens system with  $x = 0.75$ ,  $D_s = 8$  kpc and  $v_t = 50 \text{ km s}^{-1}$ , with values of  $s_{\text{det}} = 0.3, 0.2$  and  $0.1$ . Other than the slow lens-source velocity ( $\langle v_t \rangle \approx 200 \text{ km s}^{-1}$  for a Bulge microlensing event), these values are typical of a microlensing event towards the Galactic Bulge. The plot shows that most of the parameter space is excluded, but thanks to the differing power-law indices on the mass dependence, there is a small range of parameters over which repeating features should be detectable. For the parameters shown, the 'detectable region' opens up at  $M \sim 1 M_{\odot}$  and  $a \sim 1 \text{ au}$ , and widens to  $3.3 < a/\text{au} < 4.4$  by  $M = 10 M_{\odot}$ . The dependence of the limits on other parameters means that the region of detectability will get smaller, and move to larger  $a$  as the source distance grows, will get larger and move to smaller  $a$  and  $M$  as the lens moves closer to the source or the observer, and will get smaller as the relative lens-source velocity increases. A small but significant fraction of binary stars will have total masses and semimajor axes in the range of detectability (e.g. Duquennoy & Mayor 1991), especially if improved photometric accuracy can reduce  $s_{\text{det}}$ .

### 3.2 A numerical approach

In deriving analytical limits on the range of lens parameters we have had to make assumptions about the magnification pattern and strength of features. If we instead proceed numerically, we need not make these assumptions as we can determine precisely the regions of the magnification pattern where features are detectable for any given photometric accuracy. We define a detectability  $\varepsilon$  that is the probability that, for a given lens system and photometric precision, an

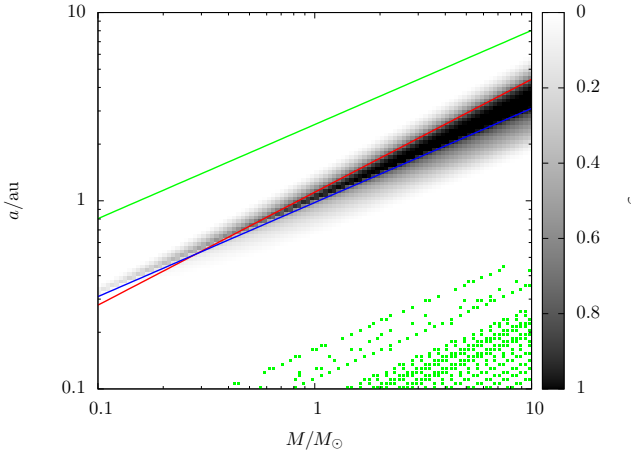


**Figure 4.** Plot of the average detectability  $\varepsilon$  against total lens mass  $M$  and semimajor axis  $a$ , for a lens with mass ratio  $q = 0.3$ . The lens and source distances and relative velocity are the same as in Figure 3. The red line is the analytical upper limit of Equation 7, while the blue line is the analytical lower limit of Equation 9 with a value of  $s_{\text{det}} = 0.28$  for a photometric precision  $\Delta m_{\text{min}} = 0.01$ . The green line at the top of the figure marks the boundary between regions of close and resonant topology lenses – we only calculate  $\varepsilon$  for close topology lenses. The green points lower in the figure mark points where our calculation of  $\varepsilon$  failed (see text for details).

RRL with a face-on orbit will exhibit at least one detectable repeating feature in its lightcurve. A feature is said to be detectable at a radial position  $u$ , if the range of magnifications  $\mu$  over a circle of radius  $u$  satisfies

$$\Delta m \equiv 2.5 \log \left[ \frac{\mu_{\text{max}}(u)}{\mu_{\text{min}}(u)} \right] \geq \Delta m_{\text{min}}, \quad (10)$$

where we have expressed the range of magnifications ( $\mu_{\text{min}} \rightarrow \mu_{\text{max}}$ ) as a magnitude difference  $\Delta m$ , and  $\Delta m_{\text{min}}$  is the photometric detection threshold, which can be taken to mean the typical uncertainty in magnitude on a data point in the baseline of the lightcurve. In calculating  $\varepsilon$  we average over the random parameters of the source trajectory and phase angle.

We can now test the predictions we made in Section 3.1, by mapping the detectability  $\varepsilon$  against total mass  $M$  and semimajor axis  $a$ , for the set of parameters we used for Figure 3. Figure 4 shows regions of finite detectability in shades of gray up to black when  $\varepsilon = 1$ . Green points in the plot show where the calculation of the detectability, which requires several numerical minimization and root finding steps, failed. The green line at the top shows the boundary between the close and resonant caustic regimes, where the three caustics of the close topology merge into a single resonant caustic. We do not calculate the detectability in the resonant regime. The red and blue lines show the analytical upper and lower limits of Equations 7 and 9, however with  $s_{\text{det}} = 0.28$  as opposed to 0.3. It can be seen in the figure that the analytical upper limit of Equation 7 agrees very well with the numerical region of detectability, coinciding with the boundary where  $\varepsilon$  begins to fall from unity with increasing  $a$  over the entire range of  $M$  shown. Equation 7, without the factor of 2 that was introduced on the left-hand side of Equation 5 to guarantee a repeated feature, also describes well the re-

gion where detection becomes possible but is not guaranteed (i.e.  $0 < \varepsilon < 1$ ).

The analytical lower limit, once the parameter  $s_{\text{det}}$  has been adjusted to 0.28 for a guaranteed repeating feature, also agrees well with the numerical region of detectability. It should be noted however, that the slope of the lower edge of the numerical region is slightly shallower than the analytical lower limit. This becomes more pronounced when the lens gets closer to the source, the total mass increases or the source velocity decreases. This is because the assumption, that there are detectable features over the entire magnification pattern within  $u < u_{\pm}$ , breaks down, and the detectable features lie in two disjoint regions, a disc surrounding the central caustic and an annulus containing the secondary caustics. The size of these regions depends on  $s$ , and the lower limit on  $a$  (Equation 9) becomes a shallower function of  $M$ . This effect is more important in determining the slope of the lower limit on  $a$  where  $\varepsilon = 0$ .

Having looked at the role of mass and orbital separation, it is important to investigate how the detectability of repeating features depends on other factors. Figure 5 shows detectability maps similar to that in Figure 4, but for a mass ratio  $q = 0.99$  and various values of the lens distance, source velocity and photometric detection threshold. The maps are arranged into four panels with different photometric threshold values of  $\Delta m_{\text{min}} = 0.005, 0.01, 0.02$  and  $0.04$  from left to right, top to bottom. Each panel is made up of a grid of  $a$ - $M$  maps showing detectability for different fractional lens distances  $x$  in each column, and different source velocities in each row. Looking first at the grid with  $\Delta m_{\text{min}} = 0.01$  (top right), it is clear that the source velocity has a large effect on the detectability, with large regions of detectability for  $v_t = 50 \text{ km s}^{-1}$  at all lens positions, which are reduced drastically for  $v_t = 100 \text{ km s}^{-1}$ . Once  $v_t = 150 \text{ km s}^{-1}$  there is only a tiny region of low detectability for lenses very close to the source (or to the observer, as  $x(1-x)$  is symmetric about  $x = 0.5$ ). For  $v_t = 200 \text{ km s}^{-1}$  there is only detectability in the most favourable cases of very high photometric accuracy and fractional lens distance. This strong dependence on  $v_t$  occurs because the number of orbits completed by the lens decreases as  $v_t$  increases (the  $v_t^{-2/5}$  term in Equation 7) but does not affect the strength of binary features (Equation 9 is independent of  $v_t$ ) – there is no cancellation of the  $v_t$  term in the ratio of upper to lower limits, while there is a partial cancellation for all the other physical parameters. Unfortunately, the microlensing event rate peaks at  $v_t \sim 200 \text{ km s}^{-1}$ , but there is a significant fraction of events with  $v_t < 100 \text{ km s}^{-1}$  (e.g. Dominik 2006).

The lens distance does not affect the size of the detectable region as strongly as the source velocity does, as the upper and lower limits of the detectable region scale with  $x(1-x)$  as similar power laws ( $-0.4$  and  $-0.5$  respectively). However, this similar scaling means that the detectable regions move as  $x$  changes, occurring at lower  $a$ , and increasing in size slightly, as the product  $x(1-x)$  decreases. For microlensing events towards the Galactic Bulge, the event rate peaks at  $x \sim 0.8$  (e.g Dominik 2006), whereas for self lensing in the Magellanic clouds  $x$  will be close to unity,  $x \approx 0.98$ .

The photometric precision of the observations strongly affects the detectability of repeating features. For  $\Delta m_{\text{min}} = 0.005$  and  $0.01$  we see large regions of detectability for small source velocities, and for  $\Delta m_{\text{min}} = 0.005$  even some de-

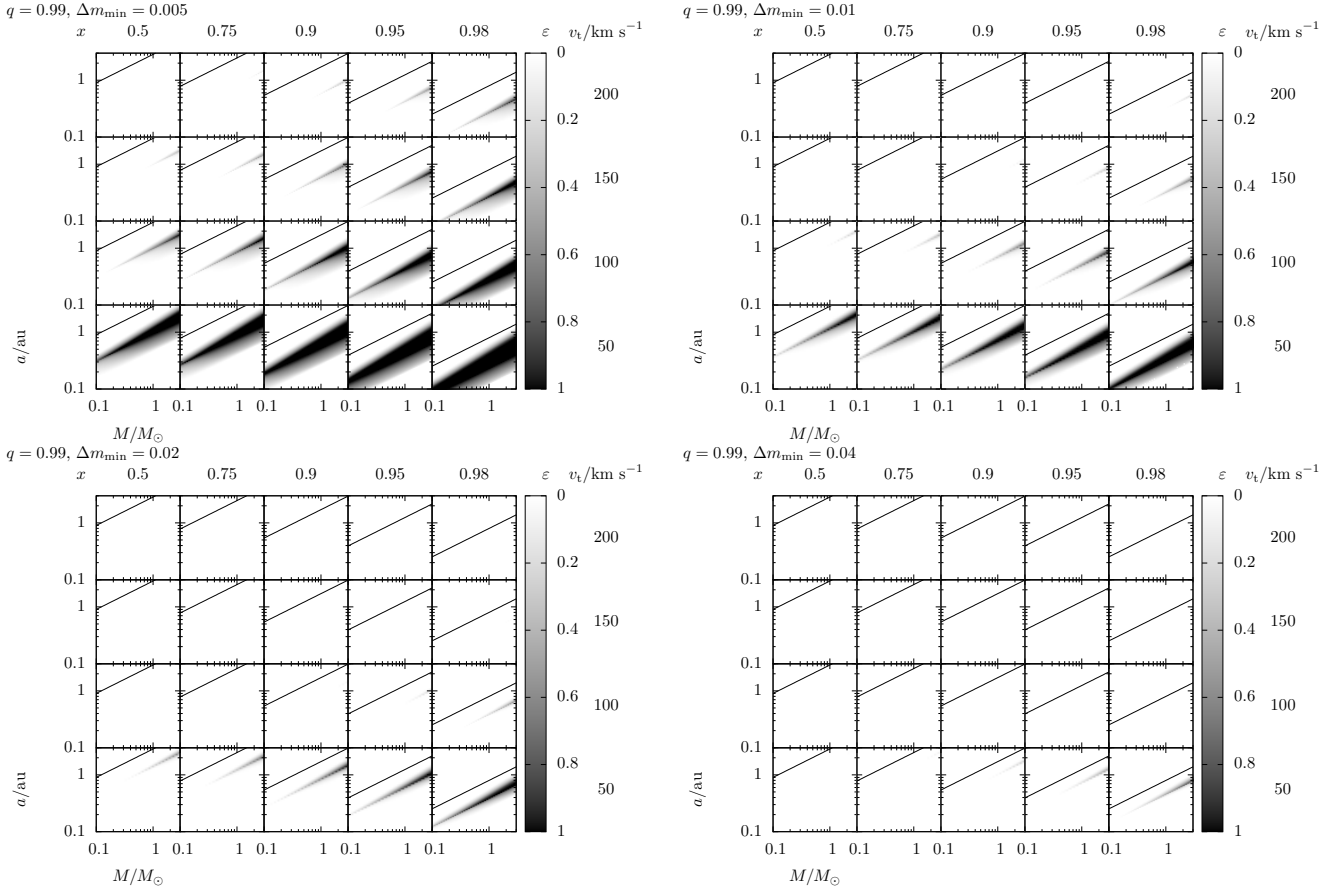
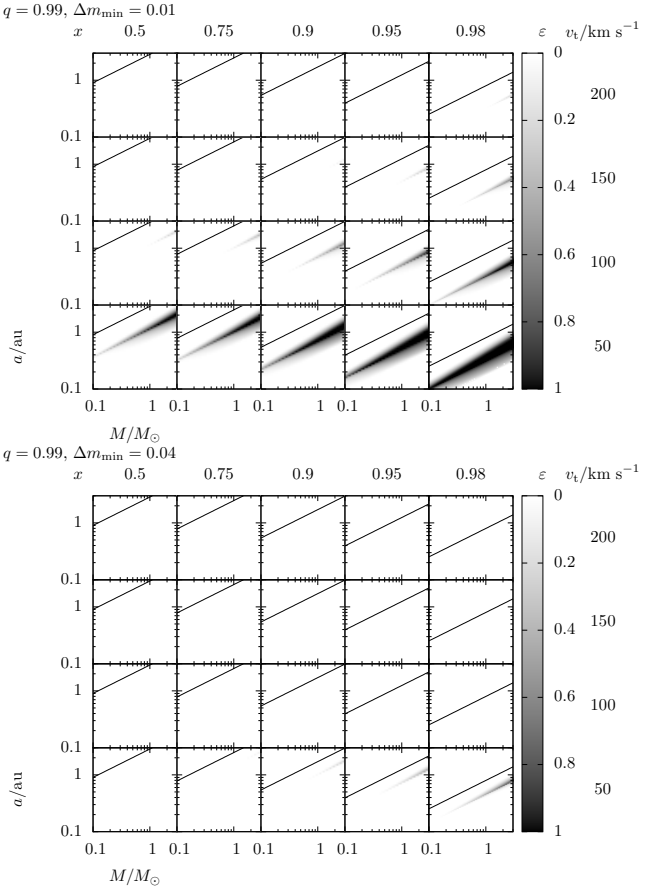


**Figure 5.** Maps of detectability  $\varepsilon$  plotted against  $a$  and  $M$  for a binary of mass ratio  $q = 0.99$  and various values of the fractional lens distance  $x = D_1/D_s$ , source velocity  $v_t$  and photometric detection threshold  $\Delta m_{\min}$ . Each small sub-panel is essentially the same as the plot in Figure 4, but with different parameter values and a slightly restricted range  $0.1 \leq M/M_{\odot} \leq 3$ ,  $0.1 \leq a/\text{au} \leq 3$ . From left to right, top to bottom panel have increasing values of the photometric threshold  $\Delta m_{\min} = 0.005, 0.01, 0.02$  and  $0.04$ . Moving from left to right, sub-panels have different fractional lens distances  $x = 0.5, 0.75, 0.9, 0.95$  and  $0.98$ ; the results remain the same under the transformation  $x \rightarrow (1 - x)$ , i.e. there is reflectional symmetry about  $x = 0.5$ . Moving from bottom to top, sub-panels have different source velocity  $v_t = 50, 100, 150$  and  $200 \text{ km s}^{-1}$ . The source distance is fixed at  $D_s = 8 \text{ kpc}$ . The black line shows the boundary between close and resonant caustic structures, above which we do not plot  $\varepsilon$ . As in Figure 4, there are points where the calculation of  $\varepsilon$  fails, but these are not shown for clarity, as they do not impinge on the regions of detectability.

tectability when  $v_t = 200 \text{ km s}^{-1}$ . As  $\Delta m_{\min}$  increases to  $0.02$ , the detectable regions shrink significantly and all but disappeared for  $v_t \geq 100 \text{ km s}^{-1}$ . For  $\Delta m_{\min} = 0.04$  there is virtually no detectability, with only a small chance of detection for the smallest velocities and largest lens distances. Increasing the threshold effectively increases the lower limit of  $a$  at which binary features are detectable, while leaving the upper limit unchanged, and like the source velocity, the photometric threshold has a large effect on the size of the detectability region. It should be noted that the detection threshold  $\Delta m_{\min}$  is in fact a combination of the effects of photometric precision and the blending by unrelated starlight, which acts to add a noise component to the measurement of the magnification caused by the lens. The effect of blending is discussed further in Appendix B1.

Even in the most favourable case of low photometric threshold and source velocity, and high fractional lens distance, the region of detectability does not reach the boundary between close and resonant caustic topologies. This is because as the projected separation increases, near the topology boundary, the secondary caustics move inwards



rapidly before merging with the central caustic, decreasing the range over which binary features are detectable. At the same time the orbital period will increase rapidly as the semimajor axis increases. These combined effects mean that in order to see repeating features from a lens with resonant topology, an extremely low source velocity is necessary to allow the lens to orbit in the time the source spends near the resonant caustic.

Figure 6 shows the same maps as Figure 5 but for differing  $q$ , and the threshold fixed at  $\Delta m_{\min} = 0.01$ . The maps for  $q = 0.3$  are similar to those for  $q = 0.99$ , and there is little difference in the size of the region of detectability. However, once  $q$  has fallen to  $0.1$ , the size of the detectable region has begun to shrink, such that for higher values of  $\Delta m_{\min}$  (not shown) there is only a very small chance of detection with small source velocities. For lower mass ratios still, there are only very small regions of detectability for  $q = 0.03$  and effectively zero detectability for  $q = 0.01$ . If we take the boundary between brown dwarfs and planets to be at  $13M_{\text{Jupiter}}$ , there is a very small region of detectability where the secondary lens is a planet, but the point of the

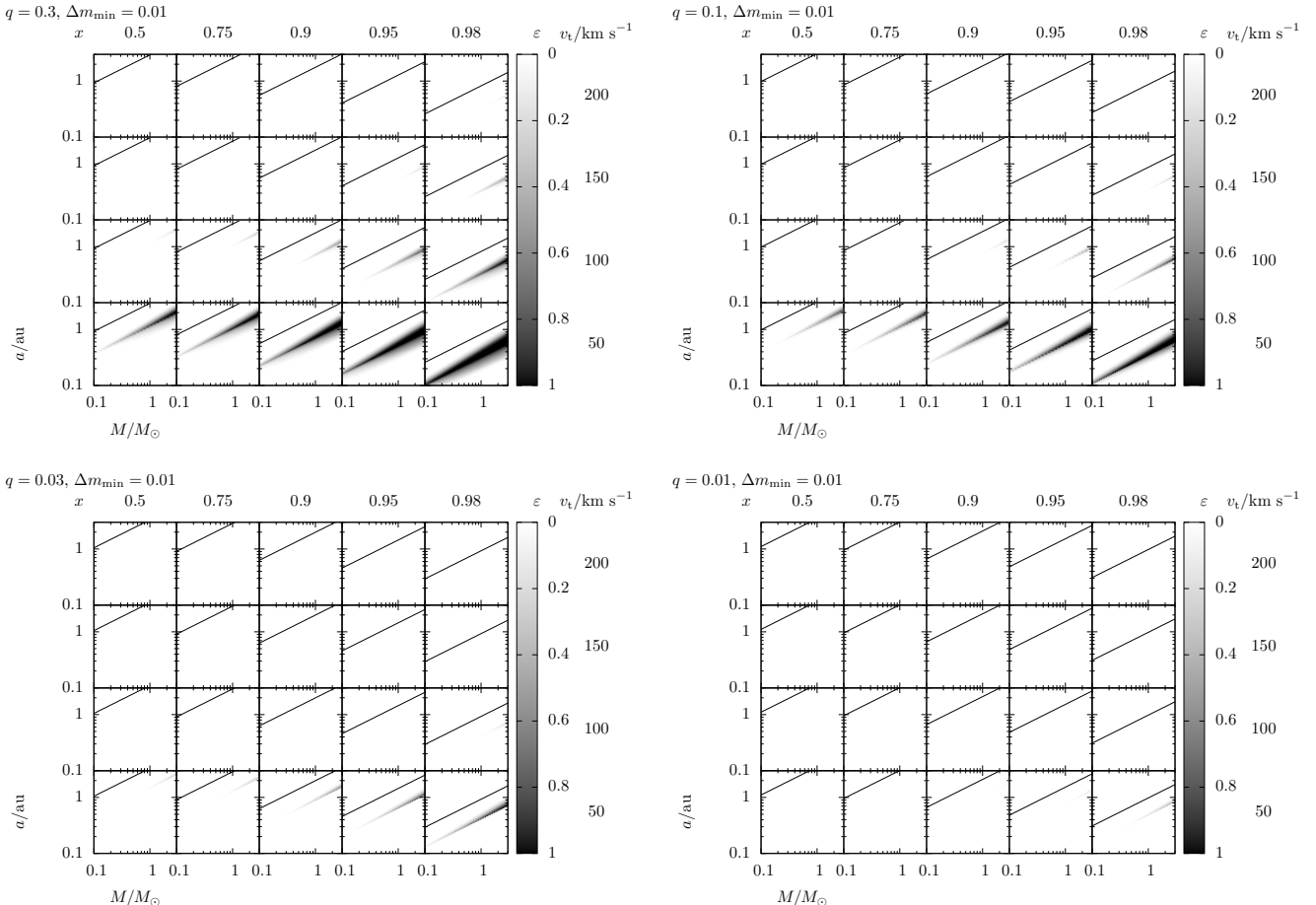


**Figure 6.** As Figure 5, but for differing mass ratios. Moving from top left to bottom right the detectability is plotted for  $q = 0.3, 0.1, 0.03$  and  $0.01$ . The total mass corresponding to a secondary below the deuterium burning limit,  $M_D \approx 13M_{\text{Jupiter}}$ , is  $M < 0.054M_{\odot}$ ,  $M < 0.14M_{\odot}$ ,  $M < 0.43M_{\odot}$  and  $M < 1.25M_{\odot}$  respectively for each value of  $q$ . The photometric detection threshold in each case is  $\Delta m_{\text{min}} = 0.01$ .

detectable region where the upper and lower limits meet occurs close to this point, regardless of the mass ratio. So, there is little chance of detecting repeating features from a planetary system, unless the photometry is very accurate, the lens very close to the source, or the source velocity is significantly smaller than  $50 \text{ km s}^{-1}$ . Such low velocity events are rare, but are known to occur, e.g. the event OGLE-1999-BLG-19 had a source velocity  $v_t = 12.5 \pm 1.1 \text{ km s}^{-1}$  (Smith et al. 2002b).

### 3.3 How many RRL events will we detect?

To estimate the RRL event rate we conducted a simulation of a space-based  $H$ -band microlensing survey, such as Euclid (Beaulieu et al. 2010) or WFIRST (Bennett 2011), and a ground-based  $I$ -band survey, based on OGLE-III (Udalski et al. 1997; Udalski 2003). Using the Besançon population synthesis model of the Galaxy (Robin et al. 2003), including a three dimensional extinction model (Marshall et al. 2006), we produced a catalogue of possible microlensing events following the recipe of Kerins et al. (2009). Source stars with magnitudes  $H_s < 25$  and  $I_s < 21$  are drawn from the Besançon model and lensed by stars of any magnitude in the space- and

ground-based simulations respectively. The lens mass is split up into two components with a mass ratio  $q$  distributed logarithmically in the range  $0.1 \leq q < 1$ , and orbit with a semimajor axis  $a$  distributed logarithmically in the range  $0.1 \leq a/\text{au} < 4$ . Each event is assigned a weighting  $w = 2r_E v_t u_{0,\text{max}}$  proportional to its event rate, where  $u_{0,\text{max}}$  is the maximum impact parameter that the event could have and its peak single lens magnification remain detected at  $5\sigma$  above baseline, taking into account blending. Each event was assigned a blending fraction  $f'_s \leq 1$  drawn from the blending distributions of Smith et al. (2007), with source density 131 stars per square arcmin, and seeing 0.7 arcsec and 1.05 arcsec for the space-based and ground-based simulations respectively. This will overestimate the blending effect for the space-based simulation, as the diffraction limited PSF for a 1 m telescope will have a full width half maximum  $\sim 0.4$  arcsec, but Smith et al. (2007) do not simulate seeing better than 0.7 arcsec. The final blending suffered by the source  $f_s$  also includes flux from the lens, which is obtained from the Besançon model assuming it is a single star. The severity of blending is thus overestimated, especially for the space-based survey, and as blending has a large effect on the detectability (see Appendix B1), the event rates we estimate will be con-

servative. However, we do not include the effect of orbital inclination, which can decrease the amplitude of lightcurve features slightly (see Appendix B3), so this optimistic assumption will likely balance the pessimistic blending we apply. The photometric detection threshold was calculated, based approximately on the proposed design of the Euclid mission (Euclid Payload Definition Document 2009) for the space-based survey, and the OGLE-III setup (Udalski et al. 1997) for the ground-based setup. Total event rates are normalized to rates  $\Gamma_{\mu L} = 7000 \text{ yr}^{-1}$  for the space-based survey (e.g. Bennett & Rhie 2002), and  $\Gamma_{\mu L} = 600 \text{ yr}^{-1}$  for the ground based survey, corresponding roughly with the OGLE-III survey. The rate of RRL events  $\Gamma_{RRL}$  is taken to be

$$\Gamma_{RRL} = \frac{\Gamma_{\mu L}}{W} \sum_i w_i \varepsilon_i, \quad (11)$$

the normalized sum of the product of  $\varepsilon_i$  and  $w_i$ , the detectability and weight of event  $i$  respectively, over all microlensing events, where  $W = \sum w_i$  again summed over all events.

The simulations do not account for the observing strategy, and assume that frequent monitoring (a few data points per night or greater) is conducted for a significant fraction of the year (6 months or greater). It is difficult to assess the impact of seasonal observability on the probability of detecting repeating features, without performing detailed detection efficiency simulations. To account for this we introduce a factor  $f_{seas}$ , the fraction of a year spent continuously observing, which is approximately the probability that an individual feature is ‘caught’. We must also account for the fact that not every lens is binary. Raghavan et al. (2010) find that 44 percent of stellar systems are multiple, with mass ratios  $q > 0.1$ , and of these about 20 percent lie in the appropriate semi-major axis range, so we adopt a binary fraction  $f_b \approx 0.1$ .

For our entire sample of space-based survey events we find that RRL events make up a fraction  $(1.1 \pm 0.2) \times 10^{-3}$  of the total microlensing event rate, which corresponds to an event rate  $\Gamma_{RRL} = (7.8 \pm 1.5) f_{seas} f_b \text{ yr}^{-1}$ . Similarly for the ground-based survey we find that a fraction  $(0.5 \pm 0.1) \times 10^{-3}$  of the total microlensing event rate is made up of RRLs, which corresponds to an event rate  $\Gamma_{RRL} = (0.32 \pm 0.06) f_{seas} f_b \text{ yr}^{-1}$ . In all cases the errors are statistical.

Figure 7 shows the distribution of microlensing timescales for the detectable RRL events and all microlensing events in the space-based simulation. The results are very similar for the ground-based survey, other than the overall normalization. The distributions do not take into account any timescale dependence on detection efficiency, or the binary fraction. The timescale distribution for RRLs shows a peak at  $t_E \sim 200 \text{ d}$  that is at timescales a factor of ten longer than the overall microlensing timescale distribution. Even at this timescale however, detectable RRL events make up less than one percent of the whole. As the timescale increases, the fraction of RRL events increases. Long timescale events are intrinsically rare, but RRL events make up a significant fraction of all events with these timescales, and so such events are good targets to search for RRL signals. Additionally, their long timescales mean that each event is observable for many years, and it is pos-

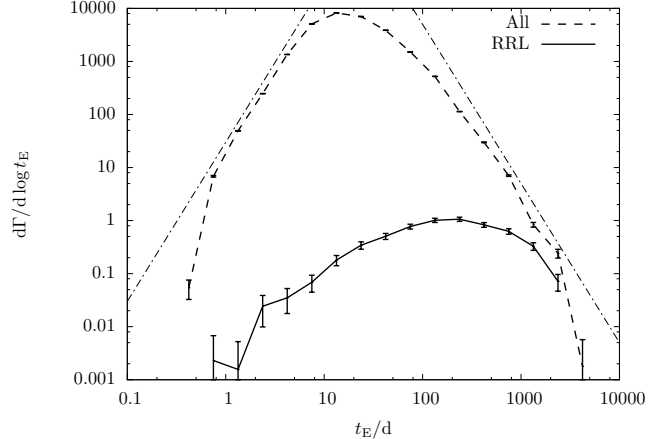


**Figure 7.** Microlensing timescale distributions for detectable RRL events (solid line) and all microlensing events (dashed line) for the space-based survey. Other than the overall normalization, the distribution for a ground based survey is very similar. The dot-dashed lines show the expected asymptotic slope of the timescale distribution, with power law indices  $\pm 3$  (Mao & Paczyński 1996)

sible to obtain dense coverage of the lightcurve with standard survey-mode observations. The timescale distribution for all events agrees well with the expected asymptotic behaviour (Mao & Paczyński 1996), except for the points at very small and large  $t_E$ , where small number statistics are in effect.

Various microlensing surveys have targeted the Galactic bulge, pretty much continuously for roughly twenty years. These survey-mode observations take place over much of the year, so the seasonal observability factor  $f_{seas}$  will be close to unity. There is therefore a good chance that there is of the order of one RRL event in current microlensing data sets. New ground based microlensing surveys, already in operation and due to start in the near future will increase the overall microlensing event rate significantly, and so there is also a reasonable chance of detecting of the order of one RRL over a timescale  $\sim 5$  years.

A space-based microlensing survey is proposed for two space missions which would launch at the end of the decade: ESA’s Euclid (Beaulieu et al. 2010) and NASA’s WFIRST (Bennett 2011). Such a mission may only spend 2–3 months per year performing a microlensing survey, as the majority of observing time would be spent on dark energy surveys. As such the seasonal observability  $f_{seas} \sim 0.2$  factor would be low, as a high degree of coincidence would be necessary for multiple RRL features to fall within the observing windows. The number of space based RRL detections is therefore likely to be low in reality. However, a dedicated space-based microlensing survey, possibly as a mission extension to Euclid or WFIRST, observing the bulge continuously for most of the year would be very likely to detect RRL events.

#### 4 PHYSICAL PARAMETERS FROM RRLS

The lightcurve of a static binary microlensing event contains information on the lens, which can be found by fitting the lightcurve with a static binary microlensing model. Simi-

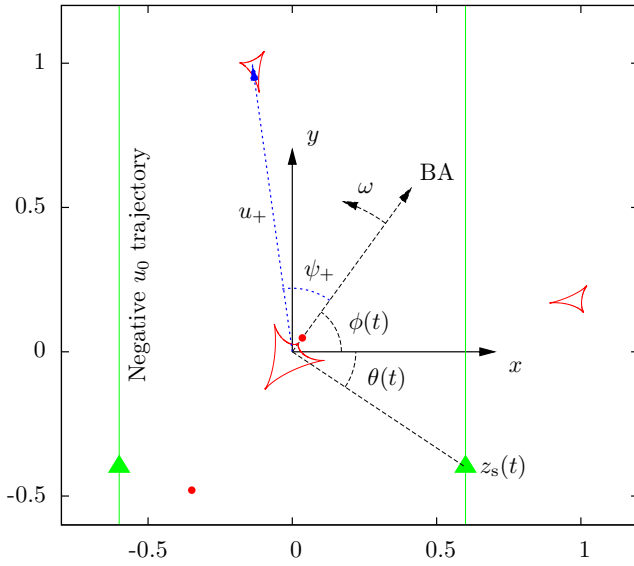


**Figure 8.** Parametrization of the rapidly rotating lenses. Causitics are shown as solid red lines, the lens positions as red circles, with the primary lens in the positive quadrant, and the source trajectory as a solid green line at positive  $x$ . The green line at negative  $x$  shows the trajectory of a source with negative  $u_0$  (see text for more details). The binary axis (BA), which subtends an angle  $\phi(t)$  relative to the fixed  $x$ -axis, rotates at a frequency  $\omega = 2\pi/T$ .  $(u_+, \psi_+)$  is the position of the secondary caustic in polar coordinates fixed to the binary axis. The blue dotted line shows the Bozza (2000) approximation to the position of the centre of the secondary caustic (Equation 18) for this lens. The lens has the parameters  $s = 0.65$  and  $q = 0.1$ , and lengths are in units of Einstein radii.

larly, the lightcurve of a rapidly rotating lens contains information about the lens and its orbit. In this section we investigate the information it is possible to extract from RRL lightcurves, and how this can be done.

The static binary lens lightcurve for a point source, can be described with a minimum of seven parameters: three to describe the source trajectory, usually an impact parameter  $u_0$  and angle  $\alpha$ , and the time of closest approach to the origin  $t_0$ ; one for the lightcurve baseline  $m_b$ ; two to describe the lens, the mass ratio  $q$  and projected separation  $s$  in units of Einstein radii; and finally the Einstein radius crossing time  $t_E$ . The coordinate system is usually chosen so that both lenses lie on the  $x$ -axis, and the origin is the centre of mass; we shall refer to it as the *static centre of mass system*.

The simplest RRL, with a face-on, circular orbit requires just one additional parameter, the orbital period  $T$ , for a total of eight parameters. In contrast, a full Keplerian orbit requires five additional parameters (including the period), bringing the total to thirteen parameters, many of which will be hard to constrain. We demonstrate below that the eight parameters of the face-on, circular model can be well constrained by the lightcurve, and parameters can effectively be ‘read off’ the lightcurve with only a small amount of algebraic manipulation. It should be possible to use these parameter estimates in a more detailed modelling analysis, either using the face-on, circular model (which will be well constrained, should the face-on, circular orbit approximation apply), or as partial constraints for a full Keplerian model. This analysis, which we describe briefly later, can

significantly reduce the range of parameters it is necessary to search in order to find a suitable event model. In Appendix B3 we briefly discuss the effects of orbital inclination and eccentricity on the lightcurves and detectability of RRLs, and in Appendix B4 we discuss the effect of parallax on an RRL lightcurve.

We choose a coordinate system fixed with respect to the sky, with its origin the lens centre of mass. As such, the lens components are not fixed. For convenience, we recast the angle  $\alpha \rightarrow \phi_0$ , where  $\phi_0$  is the angle subtended by the primary mass relative to the  $x$ -axis at time  $t_0$ , and we fix the angle of the source trajectory, such that the source travels parallel to the  $y$ -axis. At time  $t$  the source is at the (complex) position

$$z_s(t) = \left( u_0, \frac{t - t_0}{t_E} \right), \quad (12)$$

and subtends the angle

$$\theta(t) = \arctan \left( \frac{t - t_0}{u_0 t_E} \right) \quad (13)$$

with respect to the  $x$ -axis. Similarly, the binary axis, which we define as the line extending from the centre of mass through the primary mass, subtends an angle

$$\phi(t) = \frac{2\pi}{T}(t - t_0) + \phi_0 \quad (14)$$

with respect to the  $x$ -axis. This parametrization is shown in Figure 8. The parametrization differs from that recently proposed by Skowron et al. (2011) for orbiting binary lenses, which is best suited for binaries with orbits much longer than the microlensing timescale. The Skowron et al. (2011) parametrization is expressed in terms of the 3-dimensional position and velocity of one lens component, as the “on-sky” position components will be well constrained, the “on-sky” velocity components may be well constrained and the radial position and velocity are likely to be poorly or not constrained. However, as we will show, for an RRL it is the orbital period and phase angles that will be well constrained, so it is better to couch the problem in terms of these quantities.

Many of the features in a close binary lens magnification map are radial, or approximately so. This makes them ideal for measuring the rotation rate of the lens. A feature occurs on the lightcurve when a magnification pattern feature sweeps over the source. A radial feature that subtends the angle  $\psi_f$  relative to the binary axis will occur on the lightcurve when

$$\theta(t) = \phi(t) + \psi_f. \quad (15)$$

By solving this equation we can use the timing of repeated features to easily obtain approximate measurements of some of the lens parameters. This means that many of the lens parameters can be ‘read-off’ the lightcurve, and it is possible to build an approximate model of the lens quickly, without complex analysis. For such estimations, the most important magnification map features are the magnification arms (shown in Figure 1, which extend from the central caustic to the secondary caustics), and a planetary demagnification, a feature that is only present for lenses with small mass ratios, which is a region of demagnification relative to the single lens that lies between the secondary caustics, with

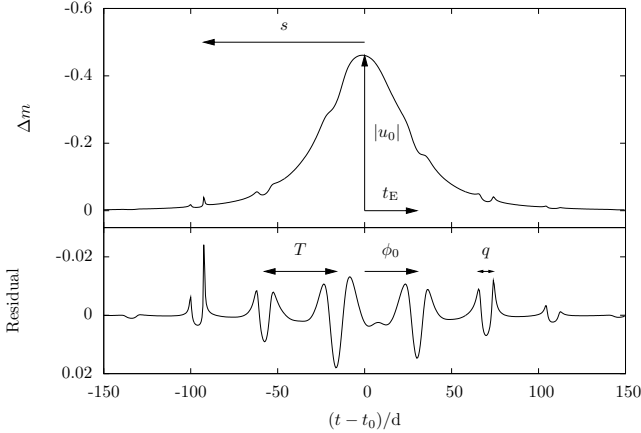


**Figure 9.** An example lightcurve by an RRL showing how lightcurve features relate to the parameters of the lens. The lens has parameters  $t_E = 30$  d,  $T = 38$  d,  $s = 0.3$ ,  $q = 0.1$ ,  $u_0 = 0.8$ ,  $\phi_0 = 2.14$

its minimum lying along the binary axis. Both features are complementary, as in equal mass ratio binaries the planetary demagnification does not occur, but the magnification arms are strong and very close to radial, while in low mass ratio binaries, the magnification arms are weaker and less radial, but the demagnification region is strong.

Figure 9 shows a lightcurve where features repeat strongly five times. The first step to estimating RRL parameters is to fit the lightcurve with a Paczyński curve. This is relatively trivial, and most RRL lightcurves will approximate a Paczyński curve with only small deviations. This fit allows an accurate estimation of the parameters  $t_0$ ,  $t_E$  and  $|u_0|$ , the last down to an ambiguity in sign, which corresponds to the source passing the lens centre on its left (positive  $u_0$ ) or right (negative  $u_0$ ) and imposing that the lens always rotates anti-clockwise. This Paczyński model completely describes the source trajectory, and hence defines the left hand side of equation 15. The orbital period can now be estimated by timing two occurrences of the same magnification pattern feature. The period is not simply the time elapsed between two features, because the source moves during this time. Instead, by solving equation 15 we can find the relation between the period  $T$ , and the time of two consecutive occurrences of the same magnification pattern feature at times  $t_1$  and  $t_2$

$$T = \frac{2\pi}{2\pi + [\theta(t_2) - \theta(t_1)]} (t_2 - t_1), \quad (16)$$

where the fraction is the number of orbits the source completes between the two source encounters. The degeneracy in the measurement of the sign of  $u_0$  affects this equation, due to the presence of the  $\theta(t)$  terms, but can be resolved if more than one pair of features is available for estimating  $T$ , as only one value of  $u_0$  will give consistent estimates of  $T$  for different feature pairs.

With an estimate of the period, if we know the angle subtended by a feature on the magnification map  $\psi_f$ , we can also estimate the phase angle  $\phi_0$ , again taking into account the source motion

$$\phi_0 = \theta(t_f) - \psi_f - \frac{2\pi}{T}(t_f - t_0). \quad (17)$$

The planetary demagnification region has  $\psi_f = 0$ , which

makes this task simple. However, the demagnification may not be obvious, or if the mass ratio of the lens is high, may not be present. In these cases it is necessary to know  $\psi_f$  for the magnification arms. Knowing that they extend from the central caustic (roughly at the centre of mass) to the secondary caustics, we need only know the position of the secondary caustics to estimate  $\psi_f$ . Bozza (2000) has derived analytical approximations to the position and shape of secondary caustics in close lenses using a series expansion of the Jacobian, critical curves and caustics for  $s \ll 1$ . He finds that the secondary caustics are located at

$$z_{\pm} \simeq \frac{1}{s(1+q)} \left[ \frac{(1-q)(1-s^2)}{\pm\sqrt{q}(2-s^2)} \right], \quad (18)$$

in the static centre of mass system. Figure 8 shows that this expression is reasonable even when  $s$  is quite large. If we assume the magnification arms are radial, we can use Equation 18 to approximate the angle of the magnification arms, to second order in  $s$ , as

$$\psi_{\pm} \simeq \arctan \left[ \frac{\pm\sqrt{q}(2+s^2)}{1-q} \right], \quad (19)$$

which is relatively insensitive to the lens separation  $s$ . It is useful to note the asymptotic behaviour:  $\psi_{\pm} \simeq \pm 2q^{1/2}$  as  $q \rightarrow 0$  and  $\psi_{\pm} \rightarrow \pm\pi$  as  $q \rightarrow 1$ . While the dependence of  $\psi_{\pm}$  on  $q$  implies an ambiguity in the estimation of  $\phi_0$ , the corollary is that we can estimate the mass ratio from the timing of features as well. Using the times of consecutive magnification arm crossings,  $t_+$  and  $t_-$ , we have

$$|\psi_{\pm}| = \frac{1}{2} \left| \theta(t_-) - \theta(t_+) - \frac{2\pi}{T} (t_- - t_+) \right|. \quad (20)$$

This value can be substituted into equation 17, and equation 19 can then be solved for  $q$ .

The remaining parameter that we are interested in is the lens separation  $s$ . The angle of features is essentially independent of  $s$ , so it is not possible to estimate  $s$  by timing features. However, by noting that the magnification pattern becomes essentially featureless beyond the secondary caustics (see Figure 1), and that the position of the caustics does depend on  $s$ , it is possible to estimate  $s$  from the lightcurve. Unfortunately the secondary caustics are very small, and in most events, they will not pass directly over the source, so the estimate will not be very accurate. The best estimate of the position of the caustic will be derived from the largest peak due to a magnification arm in the wings of the lightcurve (e.g. the peak at  $t \approx -90$  d in Figure 9). This will occur when the radial source position approximately coincides with the radial caustic position, so that  $|z_s|^2 \approx |z_{\pm}|^2$ . Using Equation 6, to first order, we can write

$$s \approx \left[ u_0^2 + \left( \frac{t_c - t_0}{t_E} \right)^2 \right]^{-1/2}, \quad (21)$$

where  $t_c$  is the time of the peak due to the caustic.

We have outlined how the parameters of an RRL can be estimated from pairs of feature timings in the case of the simplest RRL. However, in a given event there may be many repetitions, and better parameter estimates can be obtained by considering all the lightcurve features simultaneously. For a given magnification pattern and source trajectory it is possible to compute a timing model by finding all possible solutions of equation 15,  $\theta(t) = \phi(t) + \psi_f$  for each feature. By

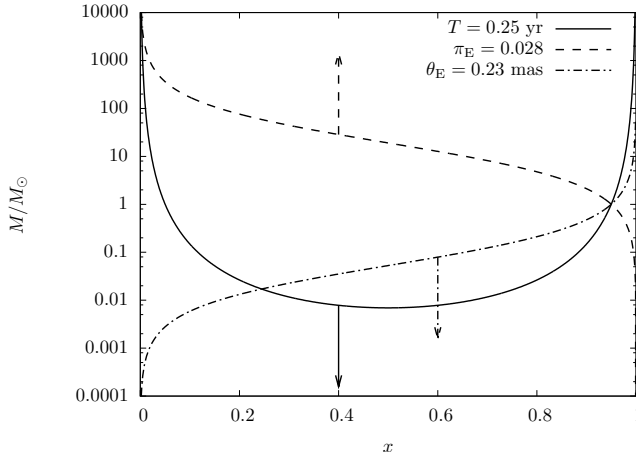


**Figure 10.** Plot of the various mass-distance relations for the event shown in Figure 9, labelled by the parameter measurement that would allow their definition. The arrows point into the region that is *allowed* should only an upper limit on  $T$ ,  $\pi_E$  or  $\theta_E$  be available. If the period  $T$  is measured along with only one of  $\pi_E$  or  $\theta_E$ , the mass and distance to the lens can not be determined uniquely, but even a relatively weak upper limit on the other parameter may be sufficient to rule out one possible solution; note however that a lack of finite-source effects places a lower limit on  $\theta_E$ .

extracting the occurrence time of all the lightcurve features it is possible to fit timing models to this timing data. It is also possible to add additional features to this timing model, such as the effects of inclination and eccentricity by modifying the function  $\phi(t)$ , or microlensing parallax by modifying  $\theta(t)$ . This modelling may be significantly faster than a full lightcurve fitting analysis, especially when additional effects are included, as there is no need to calculate finite-source magnifications. While it will not fully remove the need for lightcurve fitting, it will significantly narrow down the range of parameters over which lightcurve fitting has to search.

We have shown that it is possible to estimate the parameters of an RRL lightcurve, but what we would really like is to be able to measure the physical parameters of the lens, most importantly the lens mass and the binary separation in physical units. Compared to a static binary lens, we have one additional piece of information with which to infer  $M$  and  $a$ : the orbital period. Dominik (1998) has shown that by combining the orbital period  $T$  and the lens separation  $s$ , it is possible to write down a mass-distance relation

$$M = \frac{T^4}{C^6 s^6 x^3 (1-x)^3 D_s^3}, \quad (22)$$

which relates the mass to the lens distance through known quantities, assuming the source distance is known from its colour and magnitude; the constant  $C = 2.85 M_\odot^{-1/2}$  au kpc $^{-1/2}$  when the period is measured in years and the source distance in kpc. As demonstrated in Appendix B3 it is likely that if the orbit is inclined it will be possible to measure the inclination and account for projection, so that the value of  $s$  measured is a good approximation of  $a/r_E$ . This means that as equation 22 has a minimum at  $x = 0.5$ , we can place a firm lower limit on the mass of the lens, and an upper limit on the semi-major axis.

To improve on the mass-distance relation, an additional

piece of information is needed to break the degeneracy. This can be done by measuring  $\pi_E = au(1-x)/r_E$ , the microlensing parallax (Gould 1992), or by measuring  $\theta_E = r_E/D_1$ , the angular Einstein radius, through detection of finite-source effects (Gould 1994; Nemiroff & Wickramasinghe 1994; Witt & Mao 1994), or direct detection of the lens once it has separated from the source (Alcock et al. 2001; Bennett et al. 2006, 2007; Kozłowski et al. 2007). Measurement of either  $\pi_E$  or  $\theta_E$  allow a second mass-distance relation to be written, for  $\pi_E$  (Gould 1992)

$$M = \frac{au^2(1-x)}{C^2 x D_s \pi_E^2}, \quad (23)$$

or similarly for  $\theta_E$  (Gould 1994; Nemiroff & Wickramasinghe 1994)

$$M = \frac{\theta_E^2 x D_s}{C^2 (1-x)}, \quad (24)$$

if  $\theta_E$  is measured in mas. One of these relations can then be combined with equation 22 to yield two possible solutions to the mass and distance. This can be seen in Figure 10, which plots the mass-distance relations for the event shown in Figure 9.<sup>1</sup> The  $\pi_E$ - and  $\theta_E$ -lines cross the  $T$ -line in two places: once at the true parameter values  $x = 0.95$ ,  $M = 1M_\odot$ , and once at other values of  $M$  and  $x$  which are different for each relation. With a measurement of only one of  $\pi_E$  or  $\theta_E$ , it is not possible to uniquely determine the mass and the distance. This is likely to be the case, as finite-source effects are most likely in lenses close to the source, while parallax is most likely in lenses close to the observer. However, even a crude limit on the unmeasured parameter may be enough to rule out one possible solution; e.g. an upper limit on  $\pi_E$  from the lack of parallax effects may allow the solution with smaller  $x$  to be ruled out, or a lower limit on  $\theta_E$  from the lack of finite-source effects may allow the solution with larger  $x$  to be ruled out. Direct detection of the lens may require a very long time baseline as RRL features are most detectable in events with low lens-source proper motions. However, RRLs are more likely to be more massive than the average lens, and hence brighter, and the diffraction limit of 30–40 m class telescopes, such as the Thirty Metre Telescope (TMT),<sup>2</sup> the Giant Magellan Telescope (GMT),<sup>3</sup> or the European Extremely Large Telescope (E-ELT),<sup>4</sup> may be sufficient to resolve the lens and source in a reasonable time.

## 5 DISCUSSION AND CONCLUSION

Although the phenomena of microlensing by lenses with rapid orbital motion has been discussed in the literature previously (Dominik 1998; Dubath et al. 2007), the realities required to estimate its occurrence rate have not properly been accounted for. In this paper, we have established a firm theoretical basis for rapidly rotating lenses, and used it to estimate the range of parameters over which they are

<sup>1</sup> Note that parallax or finite-source effects were not included in the model used to plot the lightcurve

<sup>2</sup> <http://www.tmt.org>

<sup>3</sup> <http://www.gmto.org>

<sup>4</sup> <http://www.eso.org/public/teles-instr/e-elt.html>

detectable and the rate that they are expected to be observed. We find that RRLs with masses and orbital radii typical of binary stars are detectable, and that there is a reasonable chance that they will be detected, either in current microlensing data sets or in ongoing or near-future microlensing surveys.

In calculating these rates we have actually used the relatively stringent criteria of requiring that two or more lightcurve features from the same orbital phase are detected in the lightcurve. If we relax this repetition requirement somewhat, to include lenses that display significant signs of orbital motion (say several degrees rotation per  $t_E$ ), the event rate will increase significantly, as lenses can then have larger orbits and hence stronger lightcurve features. We have shown in a previous paper that orbital motion is detectable in a large fraction ( $\sim 15$  percent) of binary lenses with detectable binary lensing features and orbital periods comparable to the microlensing timescale (Penny et al. 2011).

We have detailed how the features of an RRL lightcurve can be used to measure its period and potentially measure its mass. Even if features do not repeat, if several features are detectable in the lightcurves of binary lens events, then the techniques we have outlined for timing features and extracting parameter estimates may be of some use in their analysis. Without repeating features, the orbital period may not be constrained as accurately, but it should be possible to place constraints on the lens mass and orbit in many cases.

So far, we have neglected to discuss the prospects for positively identifying RRL events from other events which may mimic their features. Periodic features may also be induced by orbital motion in the observer and source planes, or intrinsic variability in the source or a blend star. In the observer plane, the period of orbital parallax effects is well defined, and unless the lens has an orbital period similar to 1 yr it is unlikely the effects will be confused. Even if the orbital period is close to one year, the shape of features in the lightcurve are likely to be different. Orbital effects in the source plane may be more difficult to exclude, as the period is not fixed. If there is only a single luminous source (the xallarap case, Paczynski 1997; Han & Gould 1997; Rahvar & Dominik 2009), a timing analysis similar to the one we proposed for the lens can be performed for the source. This analysis is somewhat easier and more precise for xallarap as there are no complicated features in the magnification pattern. If this analysis is insufficient to separate the two cases then the shape of lightcurve features should differentiate the two interpretations. In the case where both sources are luminous, the lightcurve can take a more complicated shape, which may more closely resemble that of an RRL (e.g. Cherepashchuk et al. 1995; Han & Gould 1997). Even in this case, timing analysis for maxima and minima of the lightcurve should be easier than for RRLs, and full lightcurve modelling starting from timing analysis solutions will likely be able to differentiate the two scenarios. Finally, source variability that is not detectable at baseline, but becomes detectable with the increased photometric accuracy thanks to microlensing magnification may also produce similar lightcurve features.

It is worth noting that we should naively expect the rate of RRL/significant lens orbital motion events to be similar to the rate of binary source orbital motion events, as the factors that govern their occurrence, such as the ra-

tio of orbital separation to the Einstein ring, and the ratio of orbital to microlensing timescales will have similar distributions in the lens and source populations. Naively, we would expect the rate of parallax events to be roughly ten times greater than the rate of RRL events with orbital periods  $\sim 1$  yr, as the binary fraction is  $\sim 0.1$  while the observer is always orbiting. It is worth comparing this with the number of reported single lens parallax events,  $\sim 20$ –50 (e.g. Poindexter et al. 2005; Smith et al. 2005, and references therein), while  $\sim 10$  events have been successfully fit with xallarap models (Smith et al. 2003; Poindexter et al. 2005). In contrast, only one binary lens event has been successfully fit with a binary lens model that shows significant rotation, MACHO-97-BLG-41 (Albrow et al. 2000), which rotates at a rate  $\sim 4^\circ$  per  $t_E$ , a low rate compared to RRLs, that is detected thanks to the source crossing the central and one secondary caustic, as opposed to the smaller, more continuous features of RRLs. It is possible therefore that many events with significant rotational orbital motion signatures have not been modelled, or have been interpreted as xallarap events. It is thus important that any event that is modelled with xallarap also be tested with an orbiting binary lens model.

## ACKNOWLEDGEMENTS

We would like to thank the referee Andy Gould for helpful comments that have improved the paper. MP acknowledges the support of an STFC studentship.

## REFERENCES

- Albrow M. D. et al., 2000, *ApJ*, 534, 894
- Alcock C. et al., 2001, *Nature*, 414, 617
- An J. H. et al., 2002, *ApJ*, 572, 521
- Batista V. et al., 2011, *A&A*, 529, A102
- Beaulieu J. P. et al., 2010, in V. Coudé Du Foresto, D. M. Gelino, & I. Ribas, eds, ASP Conf. Ser. Vol. 430, Pathways Towards Habitable Planets. Astron. Soc. Pac., San Francisco, p. 266
- Beaulieu J.-P. et al., 2006, *Nature*, 439, 437
- Bennett D. P., 2011, *BAAS*, 43, 318.01
- Bennett D. P., Rhee S. H., 2002, *ApJ*, 574, 985
- Bennett D. P., Anderson J., Bond I. A., Udalski A., Gould A., 2006, *ApJ*, 647, L171
- Bennett D. P., Anderson J., Gaudi B. S., 2007, *ApJ*, 660, 781
- Bennett D. P. et al., 2010, *ApJ*, 713, 837
- Bozza V., 2000, *A&A*, 359, 1
- Buchalter A., Kamionkowski M., 1997, *ApJ*, 482, 782
- Cherepashchuk A. M., Sazhin M. V., Trifalenkov I. A., 1995, *Ap&SS*, 229, 265
- Dominik M., 1998, *A&A*, 329, 361
- Dominik M., 2006, *MNRAS*, 367, 669
- Dong S., et al., 2009, *ApJ*, 698, 1826
- Dubath F., Gasparini M. A., Durrer R., 2007, *Phys. Rev. D*, 75, 024015
- Duquennoy A., Mayor M., 1991, *A&A*, 248, 485
- Erdl H., Schneider P., 1993, *A&A*, 268, 453
- Gaudi B. S., Gould A., 1997, *ApJ*, 482, 83

Gaudi B. S. et al., 2008, *Science*, 319, 927

Gould A., 1992, *ApJ*, 392, 442

Gould A., 1994, *ApJ*, 421, L71

Gould A., Loeb A., 1992, *ApJ*, 396, 104

Griest K., Hu W., 1992, *ApJ*, 397, 362

Han C., 2009, *ApJ*, 691, L9

Han C., Gould A., 1997, *ApJ*, 480, 196

Hearnshaw J. B. et al., 2006, in Sutantyo W., Premadi P. W., Mahasena P., Hidayat T., & Mineshige S., eds, Proc. 9th Asian-Pacific Regional IAU Meeting, Institut Teknologi Bandung Press, p. 272

Hwang K. et al., 2010, *ApJ*, 723, 797

Ioka K., Nishi R., Kan-Ya Y., 1999, *Prog. Theor. Phys.*, 102, 983

Kerins E., Robin A. C., Marshall D. J., 2009, *MNRAS*, 396, 1202

Konno K., Kojima Y., 1999, *Prog. Theor. Phys.*, 101, 885

Kozłowski S., Woźniak P. R., Mao S., Wood A., 2007, *ApJ*, 671, 420

Kubas D. et al., 2005, *A&A*, 435, 941

Liebes S. J., 1964, *Phys. Rev.*, 133, 835

Mao S., Paczyński B., 1991, *ApJ*, 374, L37

Mao S., Paczyński B., 1996, *ApJ*, 473, 57

Marshall D. J., Robin A. C., Reylé C., Schultheis M., Picaud S., 2006, *A&A*, 453, 635

Nemiroff R. J., Wickramasinghe W. A. D. T., 1994, *ApJ*, 424, L21

Paczyński B., 1986, *ApJ*, 304, 1

Paczynski B., 1997, arXiv:astro-ph/9711007

Euclid Payload Definition Document, 2009, ESA Science document, SCI-PA/2008-038, issue 4, revision 2

Penny M. T., Mao S., Kerins E., 2011, *MNRAS*, 412, 607

Poindexter S., Afonso C., Bennett D. P., Glicenstein J.-F., Gould A., Szymański M. K., Udalski A., 2005, *ApJ*, 633, 914

Raghavan D. et al., 2010, *ApJS*, 190, 1

Rahvar S., Dominik M., 2009, *MNRAS*, 392, 1193

Rattenbury N. J., Bond I. A., Skuljan J., Yock P. C. M., 2002, *MNRAS*, 335, 159

Refsdal S., 1964, *MNRAS*, 128, 295

Refsdal S., 1966, *MNRAS*, 134, 315

Robin A. C., Reylé C., Derrière S., Picaud S., 2003, *A&A*, 409, 523

Ryu Y. et al., 2010, *ApJ*, 723, 81

Schneider P., Weiss A., 1986, *A&A*, 164, 237

Skowron J. et al., 2011, arXiv:1101.3312

Smith M. C., Belokurov V., Evans N. W., Mao S., An J. H., 2005, *MNRAS*, 361, 128

Smith M. C., Mao S., Paczyński B., 2003, *MNRAS*, 339, 925

Smith M. C., Mao S., Woźniak P., 2002a, *MNRAS*, 332, 962

Smith M. C. et al., 2002b, *MNRAS*, 336, 670

Smith M. C., Woźniak P., Mao S., Sumi T., 2007, *MNRAS*, 380, 805

Udalski A., 2003, *Acta Astron.*, 53, 291

Udalski A., Kubiak M., Szymanski M., 1997, *Acta Astron.*, 47, 319

Witt H. J., 1990, *A&A*, 236, 311

Witt H. J., Mao S., 1994, *ApJ*, 430, 505

Zheng Z., Gould A., 2000, *ApJ*, 541, 728

## APPENDIX A: WHAT IS HAPPENING TO THE IMAGES?

The image configuration of a point-mass lens consists of two images: a major image, of positive parity and magnification  $\mu_+ \geq 1$ , outside the Einstein ring and a minor image of negative parity and magnification  $\mu_- < 0$ , inside the Einstein ring (e.g. Refsdal 1964; Liebes 1964). The addition of a second mass to the lens causes an additional image of negative parity to be produced if the source does not lie within a caustic (Schneider & Weiss 1986). If the lens is far from resonance, i.e.  $s \ll 1$  or  $s \gg 1$ , two of the three images can still be associated with the major and minor images of the single lens, while the new third image is labelled a tertiary image.

It is interesting to study what is happening to each of the three images during the course of an RRL event. Dubath, Gasparini & Durrer (2007) study the effects of an orbiting close binary lens on the major image, by casting the lensing potential as a time varying quadrupole. They show that the major image can exhibit significant time dependent deviations from the single lens form when it is highly magnified, and go on to calculate the expected rate of events showing such deviations. Unfortunately, they neglect to treat both the tertiary image and the minor image, the latter of which will be magnified to a similar degree, as  $|\mu_+| - |\mu_-| = 1$  (e.g Refsdal 1964; Liebes 1964).

In Figure A1 we plot the lightcurves of all three images for an unrealistic lens with repeating features. In the top panel of the figure the combined lightcurve (that which would be observed) is shown in red, and the absolute magnification of the major  $|\mu_+|$ , minor  $|\mu_-|$  and tertiary images  $|\mu_3|$  is plotted in green, blue and magenta respectively. The second panel from the top shows the residual of the lightcurve relative to the lightcurve of a single lens of the same total mass, and the third and fourth panels show the absolute magnification residuals of the major and minor images with respect to their single lens counterparts; the bottom panel shows the absolute magnification of the tertiary image (note the different scale), which does not have a counterpart for the single lens. Each image shows a strikingly different pattern of features: the major image is only significantly perturbed from its single lens form when the source is within  $\sim r_E$  of the centre of mass, while the minor image shows significant perturbations out to the position of the secondary caustics. It is only when the source is close to the secondary caustics that the tertiary image is magnified significantly. However, the most important aspects in relation to the Dubath et al. (2007) event rate calculation are that firstly, the minor image can experience larger perturbations than the primary image, and secondly that the perturbations of the major and minor images are out of phase by  $\pi$ , in such a way that the peak to trough amplitude of the deviations in the total amplification lightcurve can be significantly reduced from those of the lightcurves of individual images.

## APPENDIX B: ADDITIONAL FACTORS AFFECTING RRL DETECTABILITY

In the main text we have mentioned a number of additional effects that can affect the form of an RRL lightcurve

and its detectability. Here we briefly outline the three most important effects and the impact they will have on RRL lightcurves and detectability.

### B1 Blending

For a given photometric precision  $\sigma_m$  magnitudes, the effective threshold at the event baseline is

$$\begin{aligned}\Delta m_{\min} &= 2.5 \log (10^{0.4\sigma_m} - 1 + f_s) - 2.5 \log f_s \\ &\simeq 2.5 \log \left( 1 + 0.92 \frac{\sigma_m}{f_s} \right),\end{aligned}\quad (\text{B1})$$

where the approximation applies for small  $\sigma_m$  and  $f_s$  is the fraction of the total light at baseline contributed by the unlensed source. Figure B1 shows this for various values of the photometric threshold. It is clear that only with the most accurate photometry will it be possible to detect RRL features when the blend contributes most of the flux, and for less accurate photometry,  $\sigma_m \approx 0.02$  even a small amount of blending will significantly affect the detectability of features. The effect of blending decreases as the magnification increases, but we wish to see features over the entire lightcurve, and only a small region of the lightcurve will be magnified enough to significantly reduce the effect of blending.

### B2 Finite-source effects

Figure B2 shows the lightcurve of an RRL lensing a giant source of radius  $100R_\odot$ , in comparison to the same RRL lensing a point source. The effect of the finite source on the lightcurve is clear, as it causes a wider, lower peak magnification. Whilst the lens centre of mass transits the source, there is effectively no deviation from the finite-source point-lens lightcurve, except for spikes in the residual at  $t \approx \pm 20$  d, which are characteristic of a large source crossing a small central caustic (Dong et al. 2009; Han 2009). In the wings of the lightcurve there is very little difference between the finite- and point-source lightcurves, and most of the features in the residuals have the same amplitude. Only when the source is very close to the secondary caustic is there any deviation from the point-source lightcurve in the wings. The left inset of Figure B2 shows that the peak in the finite-source lightcurve at  $t \approx -210$  d is slightly broader and about half the amplitude of the point-source lightcurve. Interestingly, this peak, although broadened by the finite-source, is still much narrower than the source crossing time, which determines the width of the central peak. Its width is instead determined by the time taken for the secondary caustic to cross a source diameter.

The example we have shown is very extreme, with a very large source, very close to the lens, and even then the finite-source effects only render binary features undetectable over a relatively small fraction of the lightcurve. A typical giant source star will be up to a factor of ten smaller, so the part of the lightcurve severely affected by finite-source effects will be correspondingly smaller. As the source has to be transited by the lens centre for finite-source effects to become apparent at the lightcurve peak, the probability of this occurring is also reduced by the same factor. This means that finite-source effects will not affect the detectability of repeating features very much. If finite-source effects are detected in an

event, the measurement of the source radius, combined with a measurement of the lens period can be used together to measure the lens mass to a two fold degeneracy (Dominik 1998).

### B3 Inclination and eccentricity

Inclination and eccentricity of the lens orbit will act to make the magnification pattern motion much more complicated, as changes in the projected lens separation cause the caustics to move and change shape (see e.g. Figures 21 and 22 of Penny et al. 2011). The effects are too complicated to investigate in detail, but it is worth considering them in brief. For a lens with a given semimajor axis, inclining the orbit should reduce the detectability of features over part of the orbit, as  $s$  decreases. Figure B3 shows the effect of inclination on the lightcurve of an RRL. It shows that inclination tends to decrease the amplitude of features, but does not completely wipe them out, even when the inclination  $i = 90^\circ$ . In this extreme case, rather than rotating, the secondary caustics move along diagonal lines as the projected separation of the lenses changes, but their angle does not, except for flips by  $\pi$  every half period. Inclination significantly changes the morphology of the lightcurve, and can also change the timing of peaks (see e.g. those at  $t \approx -300$  d), which implies that it may be possible to measure the inclination of the lens orbit from the lightcurve.

In contrast to inclination, eccentricity may increase the detectability of features. For a given semimajor axis, eccentricity can both increase and decrease the projected separation. However, Kepler's second law implies that the lens will spend longer at larger projected separations (assuming no inclination). As with inclination, eccentricity will also change the lightcurve morphology and timing of features, so it may also be possible to measure the eccentricity of the lens from the lightcurve. Simultaneously including the effects of inclination and eccentricity in the modelling of an RRL event will likely be difficult, as together they require an additional four parameters over the standard RRL parametrization. However, as the angle of magnification pattern features does not depend strongly on the projected separation, it will be possible to include inclination and eccentricity in the timing analysis proposed in Section 4, which may significantly ease the analysis by narrowing down the search space to the range of parameters compatible with timing measurements.

### B4 Parallax

Parallax effects due to the motion of the Earth about the Sun will cause the source to appear to take a curved path through the plane of the sky, and will affect the lightcurve of an RRL event. If the magnitude of the parallax effect is small then it will cause only small perturbations to the shape of the lightcurve and the timing of features. Larger effects may cause significant changes to the RRL lightcurve, significantly changing the timing of features, and possibly making them appear less periodic, or adding a stronger annual periodicity to the lightcurve. However, while parallax may significantly complicate the interpretation of an RRL event, it does not affect the magnification map, and the detectability of RRL features should remain the same. Moreover, the detection of parallax in an RRL event will allow the

lens mass to be measured, at least to a two-fold degeneracy (see Section 4). Due to the photometric accuracy required to detect RRLs, and the long timescales of the events, the probability of detecting parallax along with RRL features is significant (Buchalter & Kamionkowski 1997).

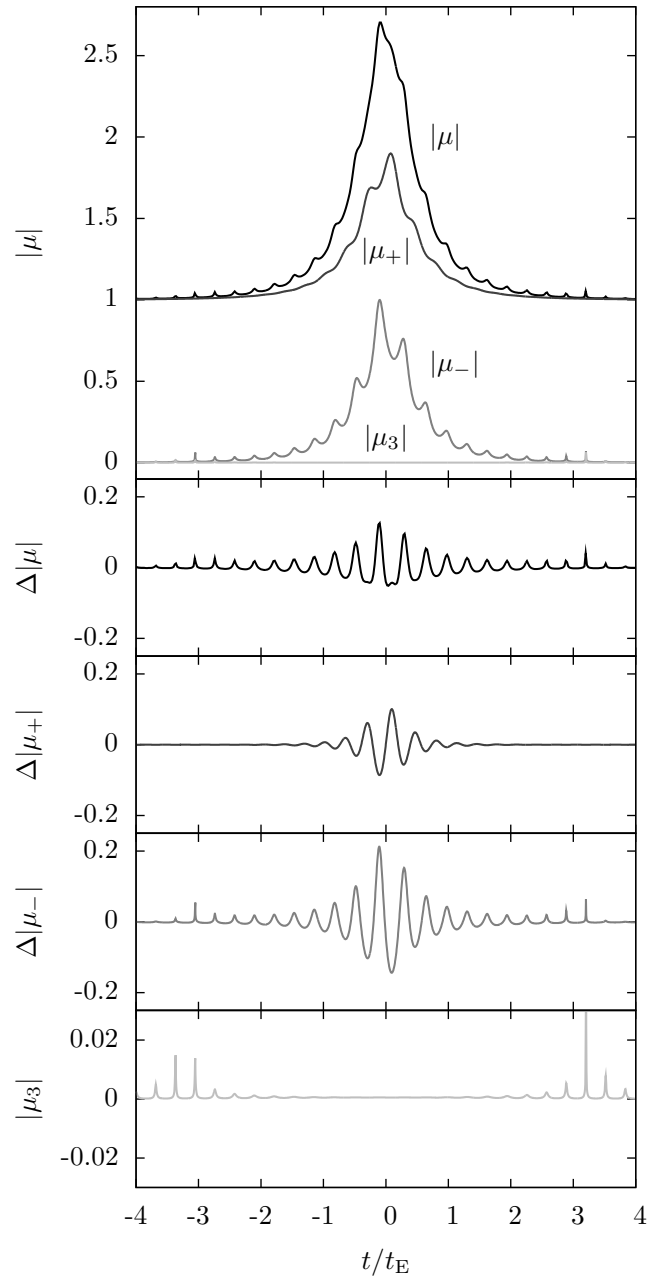


**Figure A1.** Lightcurves and residuals for each image of a microlensing event with repeating features. The top panel shows the absolute magnification of the combined images ( $|\mu|$ ), and the individual major ( $|\mu_+|$ ), minor ( $|\mu_-|$ ) and tertiary ( $|\mu_3|$ ) images in different shades of grey. The central panels show the absolute magnification residual with respect to the single lens form for all images combined, the major image and the minor image, going from top to bottom, respectively; the bottom panel shows the absolute magnification of the tertiary image, which has no single lens counterpart. The event has the unrealistic parameters  $u_0 = 0.4$ ,  $s = 0.3$ ,  $q = 1.0$  and  $t_E/T = 10$ .

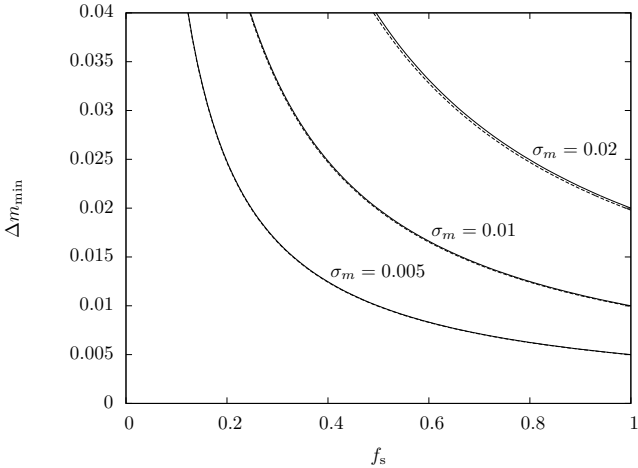


**Figure B1.** The effect of blending on the photometric detection threshold. The effective threshold  $\Delta m_{\min}$  is plotted against the ratio of source to total blend flux  $f_s$  for three values of photometric precision  $\sigma_m$ . The solid lines show the exact value, whereas the dashed line shows the approximation for small  $\sigma_m$ .

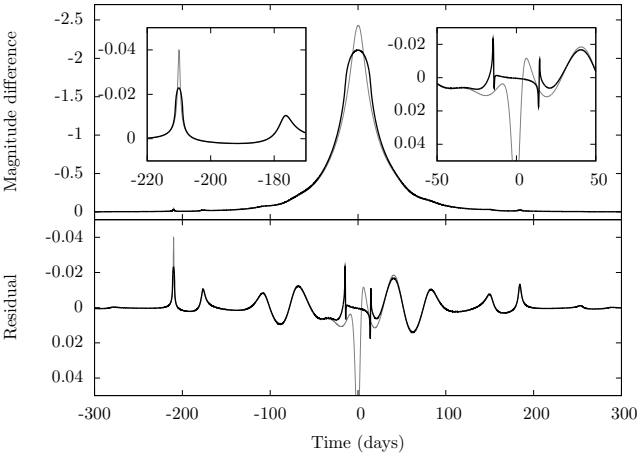


**Figure B2.** The lightcurve of an RRL lensing a finite source of radius  $100R_{\odot}$  (black) compared to the lightcurve of the same RRL lensing a point source (grey). The inset figures show in more detail the residuals when the source is close to the secondary caustic (on the left) and the central caustic (on the right). The lens has a mass  $M = 0.8M_{\odot}$ , semimajor axis  $a = 0.4$  au, mass ratio  $q = 0.3$ , fractional lens distance  $x = 0.95$ , source distance  $D_s = 8$  kpc, source velocity  $v_t = 50$  km s $^{-1}$ , impact parameter  $u_0 = 0.1$  and phase angle  $\phi_0 = \pi/4$ . The ratio of source to Einstein angular radii  $\rho_s = \theta_s/\theta_E = 0.28$  is very large. The effects of finite sources are only significant when the source is near the central or secondary caustics.

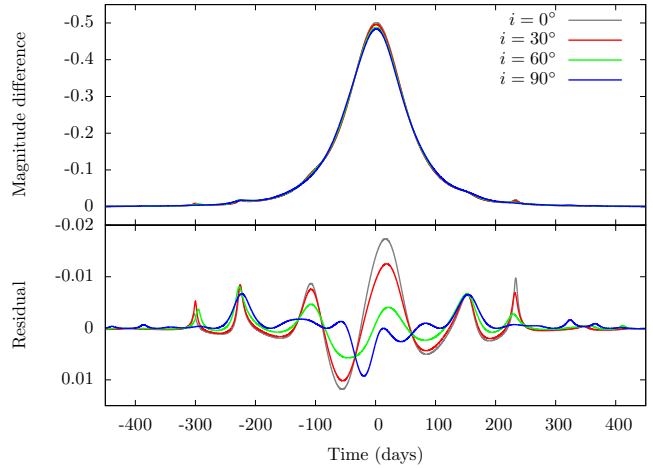


**Figure B3.** The lightcurves of RRLs with different orbital inclinations relative to the line of sight. For each lightcurve, the lens has mass  $M = 0.58M_{\odot}$ , semimajor axis  $a = 0.54$  au, mass ratio  $q = 0.52$ , fractional lens distance  $x = 0.86$ , source distance  $D_s = 9.5$  kpc, source velocity  $v_t = 61$  km s $^{-1}$ , impact parameter  $u_0 = 0.77$ , phase angle  $\phi_0 = 4.3$  measured in the plane of the orbit. The orbit was circular, and inclined about the  $x$ -axis as defined in Figure 8.